J. Am. Ceram. Soc., 71 [3] 157-66 (1988)

Microcracking in Ceramics Induced by Thermal Expansion or Elastic Anisotropy

VIGGO TVERGAARD

Department of Solid Mechanics, The Technical University of Denmark, Lyngby, Denmark

JOHN W. HUTCHINSON

Division of Applied Sciences, Harvard University, Cambridge, Massachusetts 02138

The effect of crystal anisotropy on the formation of grain-boundary microcracks is analyzed, by considering a planar array of hexagonal grains as a model of a polycrystalline ceramic. The stress singularities at triple-grain junctions are analyzed by an asymptotic method as well as by a numerical solution, and the critical size of a grain-boundary defect is investigated by a crack analysis. It is found that elastic anisotropies can significantly increase the stress levels near triple points, which results in a smaller critical grain size for microcracking.

I. Introduction

In SINGLE-PHASE polycrystalline ceramics thermal expansion anisotropy of the grains gives rise to residual stresses during cooling from the fabrication temperature, and these residual stresses can result in spontaneous cracking, primarily along grain boundaries. A number of experimental investigations[1-3] have shown that such cracking is grain size dependent. Thus, fine-grained materials do not crack, whereas some cracks are observed when the grains reach a certain critical size range, and for larger grains cracking is more severe. For a number of different ceramics Rice and Pohanka[3] have listed critical grain size values corresponding to spontaneous cracking, based on experimental observations, and they also specify the thermal expansion anisotropies.

Evans[4] and Fu and Evans[5] analyzed grain-boundary stresses due to thermal expansion anisotropy by considering a group of planar hexagonal grains embedded in an infinite isotropic elastic matrix. Various relative orientations of the thermal expansion anisotropies of the grains were considered, while the grains were taken to be elastically isotropic, thus allowing for a closed-form solution. It was found[4,5] that the stresses near a triple-grain junction exhibit a logarithmic singularity, which is clearly important in considering microcrack nucleation. For a crack on a grain-boundary facet, extending from the facet corner, Evans[4] has calculated the stress intensity factor, to estimate the critical crack length that will result in a full facet microcrack. Similar analyses and comparison with a number of laboratory studies for the effect of thermal expansion anisotropy in rocks have been presented by Fredrich and Wong.[6]

A considerable interest in the effect of microcracks in ceramics has recently been devoted to the toughening associated with a microcrack process zone around the tip of a macroscopic crack (Rühle *et al.*,[7] Hutchinson,[8] Ortiz[9]), somewhat analogous to transformation toughening in ceramics.[10] The process zone gives a redistribution of the stress field near the tip of the microscopic crack, partly due to the reduction of the effective elastic moduli resulting from microcracking, and partly due to the volume expansion arising from the release of residual stresses when microcracks are formed. In this situation the nucleation of microcracks is primarily a result of the very high stresses near the tip of the macroscopic crack, whereas the stresses further away from the tip are not large enough to nucleate microcracks. Thus, the grain size is so small that the residual stresses resulting from thermal expansion anisotropy are not sufficient to nucleate microcracks, without the additional influence of very high applied stresses.

The elastic anisotropy of the grains was incorporated into a simple model by Boas and Honeycombe,[11] who investigated the effect of thermal expansion anisotropy during cyclic heating and cooling of pure metals. According to this model the stresses are relatively insensitive to elastic anisotropy; but the model neglects a number of effects, such as stress singularities. Even in the absence of thermal contractions, elastic anisotropies of the grains can give rise to singular stress fields, which may have a significant effect on microcrack nucleation. This type of singularity is not present for isotropic elastic grains, and therefore elastic anisotropy could significantly amplify the residual stress peaks resulting from thermal contraction.

In the present paper the effect of both elastic anisotropy and thermal expansion anisotropy of the grains is investigated. The polycrystal is approximated by a planar array of grains, with different orientations of the anisotropies in each grain, and grain-boundary stresses as well as the effect of a crack in the grain boundary are investigated. The elastic anisotropies considered are not chosen to model a particular ceramic material, but the order of magnitude of the deviations from isotropy is taken to be like that found for a number of crystals.[12,13]

II. Polycrystal Model

A planar array of hexagonal grains is used as a two-dimensional model of the polycrystalline solid (Fig. 1). Each grain is assumed to be elastic orthotropic, but the orientation of the orthotropy differs from grain to grain. The grain size is specified by the length d of a grain-boundary facet.

In each grain a local Cartesian coordinate system x_i^* is chosen with axes parallel to the principal axes of the elastic orthotropy, while a global Cartesian coordinate system is denoted by x_i. The x_3^* axis is parallel to the x_3 axis for all grains in the planar array, and the rotation of the in-plane principal axes relative to the global coordinates is specified by an angle ω, defined in Fig. 1(*b*). The type of pattern of crystal orientations to be considered here is shown in Fig. 1(*a*), where the direction of the x_1^* axis is indicated for each grain. There are three different orientations, corresponding to the grains numbered 1, 2, and 3, respectively, and thus all crystal orientations for the model aggregate are specified in terms of the angles ω_1, ω_2, and ω_3. Furthermore, to retain certain symmetries, the consideration is limited to cases where $\omega_2 = 0$ and $\omega_3 = -\omega_1$, so that all crystal orientations are given by the value of a single angle ω_1 (the orientation in grains of type No. 1).

The stress–strain relations are specified for a single grain, with reference to the orthotropic axes x_i^*

$$\sigma_{ij} = C_{ijkl}(\varepsilon_{kl} - \varepsilon_{kl}^T) \tag{2.1}$$

Here, σ_{ij} is the stress tensor, ε_{kl} is the strain tensor, ε_{kl}^T are the strains resulting from thermal contraction, and C_{ijkl} is the tensor of orthotropic elastic moduli. Latin indices range from 1 to 3, Greek

Manuscript No. 199854. Received April 28, 1987. Approved October 1, 1987.
Support for J.W.H. provided in part by the Department of Solid Mechanics of the Technical University of Denmark and by the U.S. National Science Foundation under Grant No. NSF–DMR–83–16979; support for V.T. provided by the Danish Technical Research Council under Grant No. 16–4006.M.

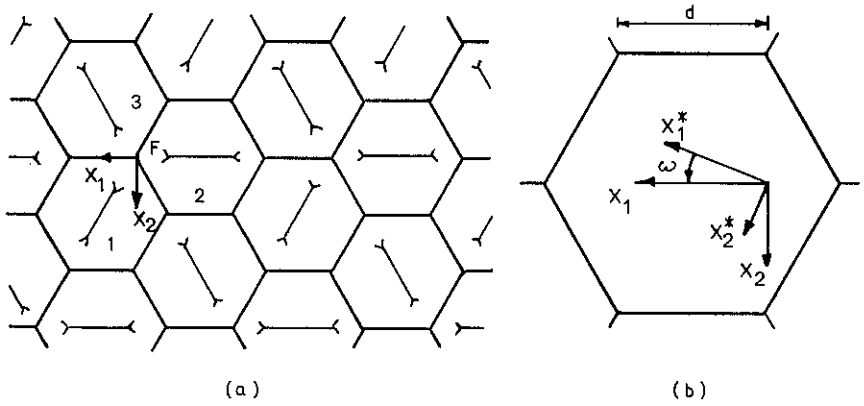

Fig. 1. (*a*) Planar array of hexagonal grains, with the direction of the x_1^* axis indicated in each grain. (*b*) Principal axes of the anisotropies are in the x_α^* directions.

indices (to be used subsequently) range from 1 to 2, and the summation convention is used for repeated indices. Because of orthotropy, $C_{1211} = C_{1222} = 0$, and in some of the following discussion the nonzero in-plane components are denoted by $C_{1111} = C_{11}$, $C_{2222} = C_{22}$, $C_{1122} = C_{12}$, and $C_{1212} = C_{44}$.

The thermal contraction ε_{kl}^T results from cooling below the fabricaton temperature. When ΔT denotes the cooling range and α_{kl} is the tensor of linear thermal expansion coefficients, the thermal contraction strains are given by

$$\varepsilon_{kl}^T = -\Delta T \alpha_{kl} \tag{2.2}$$

It will be assumed here that the thermal expansion anisotropy has the same principal axes as the elastic orthotropy. Then, on the x_i^* axes $\alpha_{12} = 0$, and the nonzero in-plane components are denoted by $\alpha_{11} = \alpha_1$ and $\alpha_{22} = \alpha_2$.

When the aggregate is subject to thermal contraction, an assumption of plane strain ($\varepsilon_{33} \equiv 0$) would give rise to unrealistically high tensile stresses σ_{33}. Instead, generalized plane strain will be assumed, with the uniform strain $\varepsilon_{33} \equiv \varepsilon_{33}^T$ in the x_3 direction, so that the contribution of thermal contraction to the average value of σ_{33} is essentially relaxed. With this assumption the in-plane part of the stress–strain relations (2.1) takes the form

$$\sigma_{\alpha\beta} = C_{\alpha\beta\gamma\delta}(\varepsilon_{\gamma\delta} - \varepsilon_{\gamma\delta}^T) \tag{2.3a}$$

$$\varepsilon_{\gamma\delta}^T = -\Delta T \alpha_{\gamma\delta} \tag{2.3b}$$

It is noted that choosing a uniform strain ε_{33} different from ε_{33}^T would result in constant stresses σ_{11}^T and σ_{22}^T to be added to the right-hand side of Eq. (2.3*a*).

For the analysis of the stress distribution in the full polycrystal the stress–strain relationship written with reference to the global x_i coordinates is needed. This relationship is still of the form of Eqs. (2.3), but the elastic moduli and the thermal expansion coefficients have to be transformed. For a grain characterized by the angle ω between the local and global coordinates (Fig. 1(*b*)), the tensor of elastic moduli $C_{\alpha\beta\gamma\delta}^\circ$ and the thermal expansion tensor $\alpha_{\gamma\delta}^\circ$ on the x_i coordinates are given by

$$C_{\alpha\beta\gamma\delta}^\circ = C_{\lambda\mu\omega\zeta} l_{\lambda\alpha} l_{\mu\beta} l_{\omega\gamma} l_{\zeta\delta} \tag{2.4a}$$

$$\alpha_{\gamma\delta}^\circ = \alpha_{\lambda\mu} l_{\lambda\gamma} l_{\mu\delta} \tag{2.4b}$$

$$l_{11} = l_{22} = \cos\omega \tag{2.4c}$$

$$l_{21} = -l_{12} = \sin\omega \tag{2.4d}$$

The special orientations of the crystals indicated in Fig. 1(*a*) correspond to choosing $\omega_1 = -60°$. This configuration has the property that the macroscopic response of the aggregate is isotropic (the same is true for $\omega_1 = 60°$). Note in Fig. 1(*a*) that the aggregate is symmetric about the x_1 axis, and about other similar lines parallel to the x_1 axis. Note also that rotation of the whole aggregate around point F in Fig. 1(*a*), by either 120° or −120°, gives a configuration identical with that shown in the figure. Therefore, the macroscopic elastic moduli are identical for the x_1 axis pointing in any of these three directions, and it is easily proved that in such circumstances the macroscopic response is isotropic in the plane.

The present investigation will focus on the stress distributions at symmetric tilt grain boundaries, such as those on the x_1 axis in Fig. 1(*a*). Also the influence of a small crack at such symmetric boundaries will be analyzed. Although this symmetry is satisfied for any choice of the angle $\omega_1 = -\omega_3$, the investigation here is concentrated on the cases where the in-plane macroscopic elastic response is isotropic.

One particular crystal anisotropy to be considered is defined by

$$C_{11} = fC_{11}' \tag{2.5a}$$

$$C_{22} = \frac{1}{f} C_{22}' \tag{2.5b}$$

$$C_{12} = C_{12}' \tag{2.5c}$$

$$C_{44} = C_{44}' \tag{2.5d}$$

where C_{11}', C_{22}', etc., denote isotropic elastic constants. The amount of thermal expansion anisotropy is specified by

$$\Delta\alpha = \frac{1}{2}(\alpha_1 - \alpha_2) \tag{2.6}$$

Thus, all anisotropies in this case are given by the values of three parameters—f, $\Delta\alpha$, and ω.

Also cubic crystals will be considered. In this case there is no thermal expansion anisotropy, $\Delta\alpha = 0$ (as was used in the experiments of Boas and Honeycombe[11] to show the difference from other types of crystals). Here, two nondimensional parameters, R and Q, are used to characterize the cubic material

$$C_{11} = C_{22} \tag{2.7a}$$

$$R = \frac{C_{12} + 2C_{44}}{C_{11}} \tag{2.7b}$$

$$Q = \frac{2C_{44}}{C_{12}} \tag{2.7c}$$

where $R = 1$ identifies an isotropic material.

III. Stress Singularity at a Grain-Boundary Triple-Point Junction

Where three or more elastically anisotropic grains come together along a line junction, the stress field becomes singular whether due to thermal stressing or overall applied stress. The nature of the singularity depends on the geometry at the junction and on the elastic anisotropies of the grains. In some instances the stresses may be unbounded, in others the stresses may go to zero at the junction with unbounded gradients. Examples will be analyzed which illustrate a variety of possibilities. Anisotropy of the coefficients of thermal expansion in the absence of elastic anisotropy generally results in stresses, which are logarithmically infinite at the junction when the polycrystal is subject to temperature

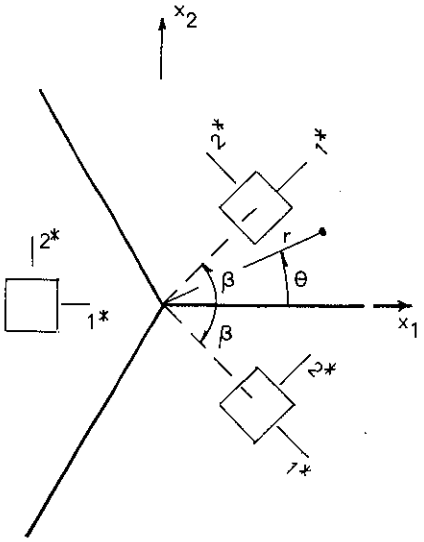

Fig. 2. Geometry at triple-point junction.

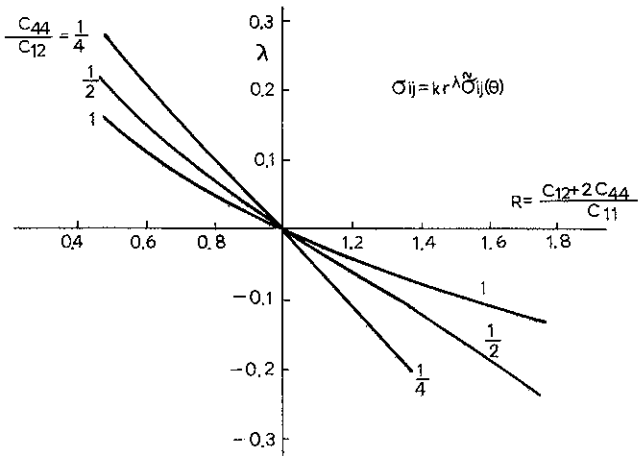

Fig. 3. Exponent of the r variation of the most singular nonhydrostatic eigenfield for cubic crystals with $\beta = 60°$.

change.[5] In this section we focus on the effect of elastic anisotropy on the form of the singularity at the junction in the absence of thermal stressing. When the singularity due to elastic anisotropy is stronger than logarithmic, that singularity will generally be dominant even in the presence of thermal stressing. In subsequent sections we will carry out the full coupled stress analysis.

Consider the triple-point junction of the plane strain hexagonal grain model shown enlarged in Fig. 2. Within each 120° sector the crystal moduli are uniform and orthotropic, or possibly cubic, in the crystal axes (the axes marked * in Fig. 2) with

$$\sigma_{11} = C_{11}\varepsilon_{11} + C_{12}\varepsilon_{22} \tag{3.1a}$$

$$\sigma_{22} = C_{12}\varepsilon_{11} + C_{22}\varepsilon_{22} \quad \text{(crystal axes)} \tag{3.1b}$$

$$\sigma_{12} = 2C_{44}\varepsilon_{12} \tag{3.1c}$$

The crystals are oriented symmetrically with respect to the x_1 axis in Fig. 2, with the crystals in the first and third sectors oriented at $\pm\beta$. It is noted that this corresponds to considering point F in Fig. 1, when $\beta = -\omega_1 = \omega_3$. We will primarily confine attention to stress fields which are symmetric with respect to the x_1 axis.

The singular stress field at the junction is amenable to a Williams-type[14] singularity analysis, which is outlined in the Appendix. The form of the stress variation associated with each eigencontribution is

$$\sigma_{ij} = kr^{\lambda}\tilde{\sigma}_{ij}(\theta) \tag{3.2}$$

where r and θ are polar coordinates centered at the junction in Fig. 2. The local singularity analysis provides λ and $\tilde{\sigma}_{ij}(\theta)$, but not the amplitude factor k, which must be obtained from an analysis of the full problem.

For the first example, take the crystals to be cubic ($C_{11} = C_{22}$) and, for the moment, take $\beta = 60°$ so that 120° symmetry exists at the junction; let R in Eq. (2.7b) be the measure of planar anisotropy of the single crystals, with $R = 1$ corresponding to isotropy.

A polycrystal of cubic crystals (planar or three-dimensional) experiences a uniform hydrostatic stress when subject to a macroscopic hydrostatic field. This means that one eigenfield always exists with $\lambda = 0$ and $\tilde{\sigma}_{ij}(\theta) = \delta_{ij}$. That is

$$\sigma_{ij} = k\delta_{ij} \tag{3.3}$$

is always a solution to the equations of the singularity analysis for cubic crystals at any junction. The exponent λ of the most singular nonhydrostatic eigenfield of Eq. (3.2) is plotted as a function of R for several values of C_{44}/C_{12} in Fig. 3. The search for the most singular eigenfield is limited to values of λ greater than -1, to ensure bounded strain energy. When $R > 1$, λ is negative and the stresses at the junction will be unbounded except under pure hydrostatic loading. However, when $R < 1$, λ is positive and the nonhydrostatic contribution to the stresses at the junction go to zero. Sufficiently near the junction one must expect the stresses to be of the form of Eq. (3.3) when $R < 1$.

Representative θ variations, $\tilde{\sigma}_{ij}(\theta)$, associated with the eigenfields are shown in Figs. 4(a) and (b). In this instance (because of the symmetries) there is both a symmetric and an antisymmetric field associated with the same λ. Only the symmetric field with respect to x_1 is shown. Continuity of tractions across the grain boundary at $\theta = 120°$ requires $\tilde{\sigma}_{\theta\theta}$ and $\tilde{\sigma}_{r\theta}$ to be continuous across $\theta = 120°$; $\tilde{\sigma}_{rr}$ is discontinuous, as is $d\tilde{\sigma}_{r\theta}/d\theta$. The variations $\tilde{\sigma}_{ij}(\theta)$ have been normalized by taking $\tilde{\sigma}_{\theta\theta} = 1$ at $\theta = 0$.

An example illustrating the influence of the crystal orientation β on the exponent λ for the cubic case is shown in Fig. 5. For β less than 30°, unbounded stresses occur when $R < 1$ rather than $R > 1$. Thus, it is seen that whether or not the stresses at a triple-point junction become unbounded depends not only on the nature of the crystal anisotropy but also on details of the geometry.

Next consider crystals with planar orthotropy ($C_{11} \neq C_{22}$) and take $\beta = 60°$, so that 120° symmetry exists at the junction. In this case the simple hydrostatic field of Eq. (3.3) is not an eigensolution, so we have obtained the two lowest, physically relevant exponents λ of eigenfields. These are shown as a function of the orthotropy measure $(C_{11} - C_{22})/2C_{44}$ in Fig. 6. In this particular example, the moduli are taken to be specified by Eqs. (2.5), and the isotropic reference moduli C'_{11}, C'_{22}, etc., in Eqs. (2.5) correspond to Poisson's ratio, $\nu = 0.2$. Thus, for any value of the parameter f in Eqs. (2.5a) and (2.5b), the ratios

$$\frac{C_{12}}{C_{44}} = \frac{2}{3} \tag{3.4a}$$

$$\frac{C_{11}C_{22}}{C_{44}^2} = \frac{64}{9} \tag{3.4b}$$

are held constant.

In this example, the stresses associated with the eigenfields are unbounded (i.e., $\lambda < 0$) at the junctions when $C_{11} > C_{22}$, but go to zero (i.e., $\lambda > 0$) when $C_{11} < C_{22}$. Evidently, increased stiffness in the circumferential direction ($C_{11} < C_{22}$) tends to isolate the junction. The 120° symmetry at the junction gives rise to special symmetries in the eigensolutions. The stress field associated with the λ values on the curve labeled "single eigenfield" in Fig. 6 has 120° symmetry as can be seen in Fig. 7. This field is the counterpart of the hydrostatic field of Eq. (3.3) in the cubic case. The other eigenvalue λ, plotted as the curve labeled "double eigenfield," has both a symmetric and an antisymmetric stress field associated with it. The symmetric field is displayed in Fig. 8 for one set of the moduli.

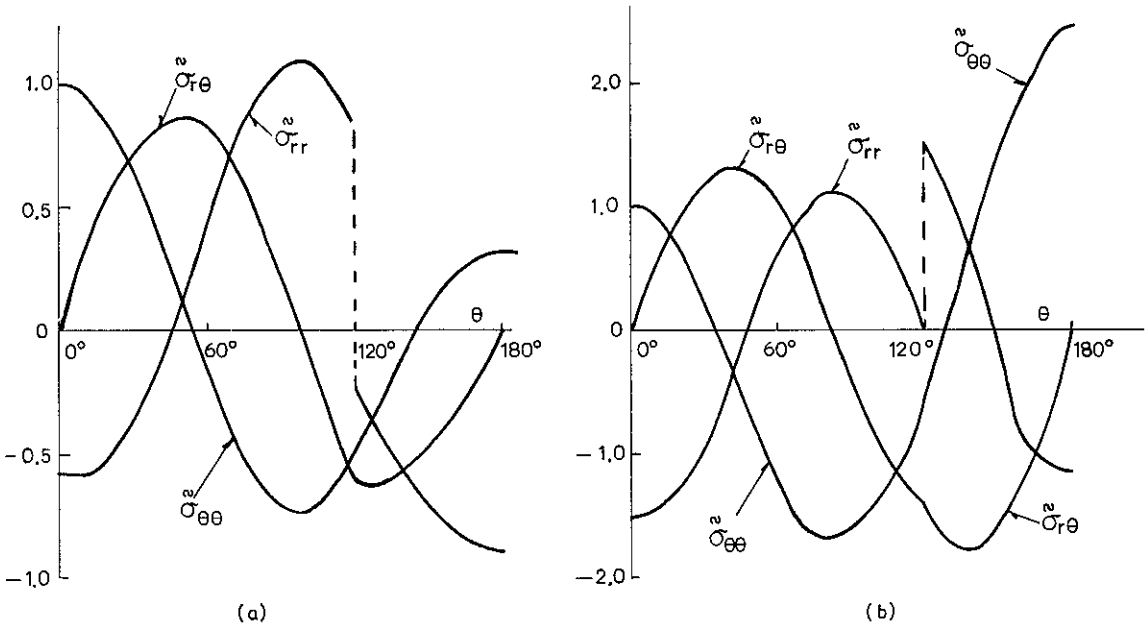

Fig. 4. Variations of $\tilde{\sigma}_{\eta}(\theta)$ for symmetric eigenfield for cubic crystals with $\beta = 60°$: (*a*) $C_{44}/C_{12} = 0.5$ and $R = 1.5$; (*b*) $C_{44}/C_{12} = 0.5$ and $R = 0.5$.

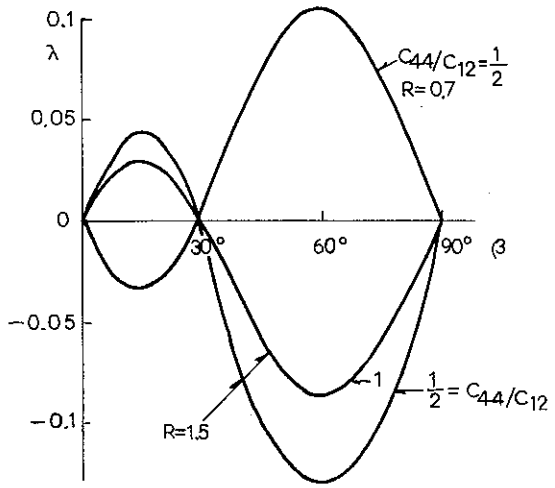

Fig. 5. Exponent of r variation of the most singular non-hydrostatic eigenfield for cubic crystals as a function of the orientation β.

The examples discussed above are far from being exhaustive. Nevertheless, they do suggest that a triple-point junction can be a vicinity of significant stress concentration, or, depending on the anisotropies and the crystal orientation, a region of lowered stress. It will be seen that these implications from the local singularity analysis are borne out by the full stress analysis for the two-dimensional polycrystalline model.

IV. Numerical Analysis of Stresses

In a numerical solution for the stress state inside the grains it is advantageous to make use of the periodicity of the grain distribution and crystal orientations shown in Fig. 1(*a*). The aggregate is assumed to be subject to a cooling range ΔT and to external in-plane loads such that the average stresses are Σ_{11} and Σ_{22}, while the average shear stress is zero, $\Sigma_{12} = 0$. Then there are symmetries, such that the stress and strain states inside one of the triangles indicated in Fig. 9(*a*) are identical with those inside each of the other triangles (note that the pattern remains identical after 180° rotations around any triangle corner, or after translation of any corner into another). Therefore, it is only necessary to analyze one triangle, as that shown in Fig. 9(*b*).

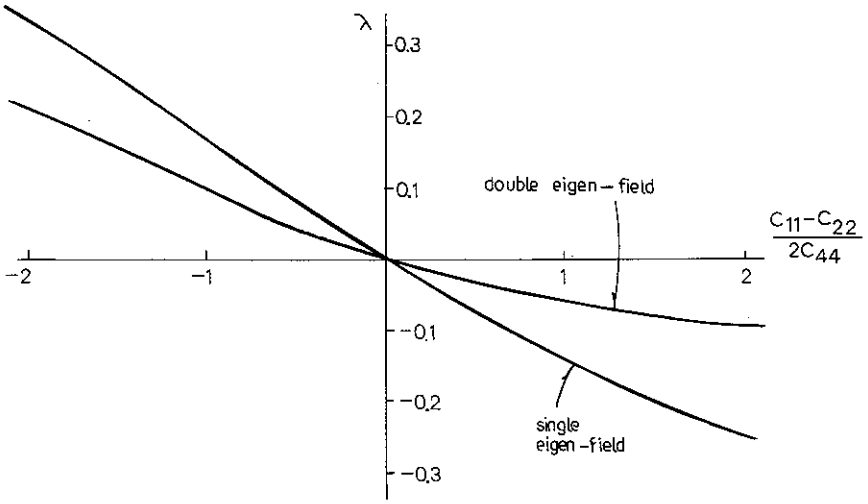

Fig. 6. Exponent of the r variation of the two most singular, physically relevant eigenfields for orthotropic single crystals with moduli specified by Eqs. (2.5) and (3.4), and $\beta = 60°$.

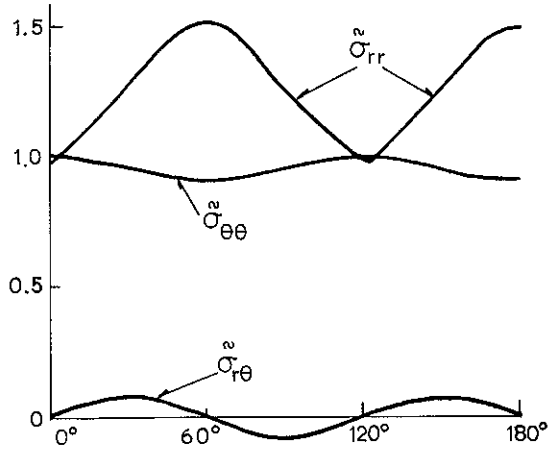

Fig. 7. Variations of $\tilde{\sigma}_{ij}(\theta)$ associated with the eigenvalue with a single eigenfield: $(C_{11} - C_{22})/2C_{44} = 2$ in Fig. 6, where $\lambda = -0.251$.

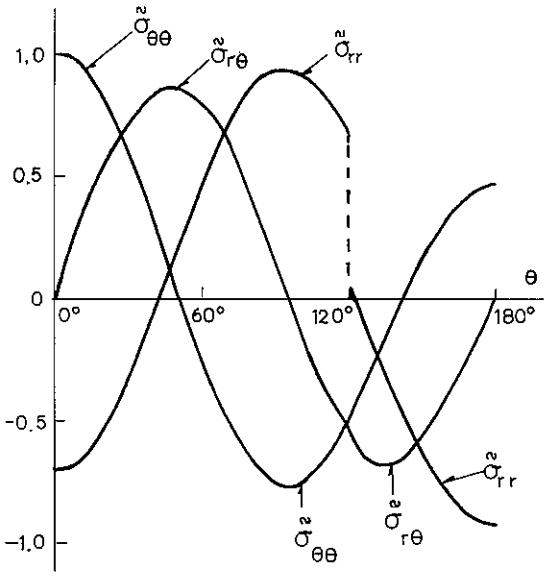

Fig. 8. Variations of $\tilde{\sigma}_{ij}(\theta)$ for the symmetric field associated with the eigenvalue with a double eigenfield: $(C_{11} - C_{22})/2C_{44} = 2$ in Fig. 6, where $\lambda = -0.091$.

The requirement of equilibrium is specified in terms of the principle of virtual work

$$\int_V \sigma_{\alpha\beta}\delta\varepsilon_{\alpha\beta}\, dV = \int_S T_\alpha\, \delta u_\alpha\, dS \tag{4.1}$$

where V and S are the volume and surface, respectively, of the body analyzed, u_α are the displacement components in the x_α-coordinate directions, and T_α are the components of the surface tractions. When the stress–strain relations of Eqs. (2.3) are substituted, referred to the global x_α coordinates of Eqs. (2.4), the equilibrium requirement of Eq. (4.1) takes the form

$$\int_V C^{\circ}_{\alpha\beta\gamma\delta}\varepsilon_{\gamma\delta}\delta\varepsilon_{\alpha\beta}\, dV = \int_S T_\alpha \delta u_\alpha\, dS - \int_V C^{\circ}_{\alpha\beta\gamma\delta}\alpha^{\circ}_{\gamma\delta}\Delta T\delta\varepsilon_{\alpha\beta}\, dV \tag{4.2}$$

where the last term on the right-hand side represents the effect of thermal contraction.

The boundary conditions to be specified for the triangular region ABC in Fig. 9(b) represent symmetry on the side AB

$$T_1 = 0, \quad u_2 = 0 \quad (\text{at } x_2 = 0) \tag{4.3}$$

The conditions on AC and BC are such that equilibrium and compatibility with the neighboring triangles are satisfied. This is expressed by using the length-measuring coordinates ξ and η on AC and CB, respectively (Fig. 9(b))

$$u_1(\xi) - u_1^A = u_1(\eta) - u_1^C \tag{4.4}$$

$$u_2(\xi) - u_2^A = -u_2(\eta) + u_2^C \tag{4.5}$$

$$T_1(\xi) = -T_1(\eta) \tag{4.6}$$

$$T_2(\xi) = T_2(\eta) \tag{4.7}$$

Here, u_α^A and u_α^C denote the displacement components at points A and C, where $u_2^A = 0$ according to Eqs. (4.3), and the value of u_1^C is a parameter to be chosen. The values of the two remaining displacement components u_1^A and u_2^C are calculated such that the average stresses are as specified

$$\Sigma_{11} = \frac{2}{3\sqrt{3}d}\int_0^{3d} T_1(\xi)\, d\xi \tag{4.8a}$$

$$\Sigma_{22} = \frac{2}{3d}\int_0^{3d} T_2(\xi)\, d\xi \tag{4.8b}$$

An approximate solution of the equilibrium equation (4.2) is obtained by the finite-element method, using the boundary conditions (4.3) to (4.8). The element approximation of the displacement components is based on eight-noded isoparametric elements, and the integrations in Eq. (4.2) are carried out using 3×3 point Gaussian quadrature within each element. In the solutions a special Rayleigh–Ritz finite-element method (Tvergaard[15]) is used to incorporate the periodicity conditions (4.4) to (4.8). The mesh used for the analyses consists of 14×6 elements, as shown in Fig. 10, where it is noted that no element crosses a grain boundary. The mesh is strongly refined near the triple-grain junction denoted by F in Fig. 1(a), since the present work will focus on the stress

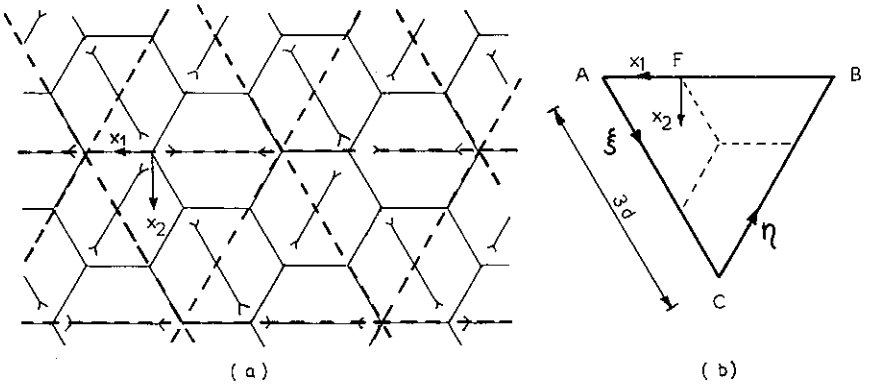

Fig. 9. (a) Dashed lines indicate triangles inside which stress and strain states are identical. (b) The triangular region analyzed.

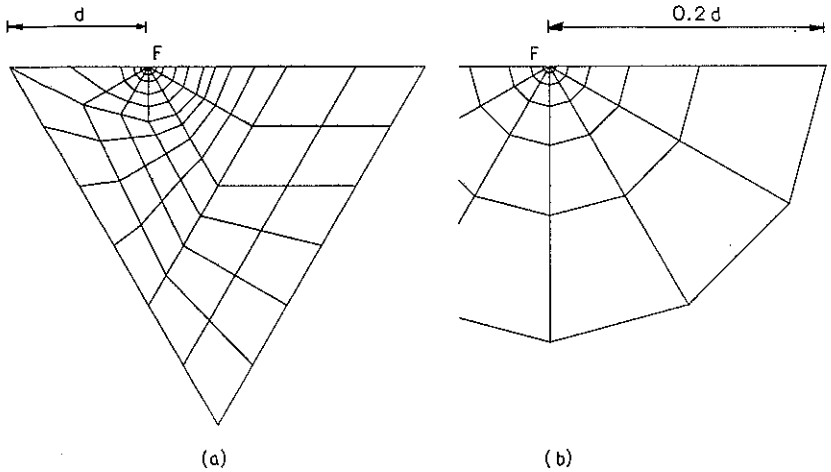

Fig. 10. (*a*) Mesh used for the numerical analysis. (*b*) Mesh near the triple-grain junction *F*.

concentrations at this particular type of triple-grain junction. The six elements in the first ring around the triple point are wedge shaped, so that one side is collapsed to a point, and the 13 nodes meeting at the triple point are tied together as a single node (analogous to crack tip elements, Shih and Needleman[16]).

Isotropic elastic grains have been analyzed under various external loads or temperature changes, to test that the numerical solution does give the appropriate uniform stress and strain fields. Furthermore, the uniaxial plane strain tension modulus $\bar{E}$ of the aggregate has been calculated for a number of anisotropies ($\Sigma_{22} = \bar{E}\varepsilon_{22}$ for tension in the x_2 direction), since this modulus will be used for normalization in some of the following diagrams. For anisotropy orientations characterized by $\omega_1 = -60°$, where the macroscopic response of the aggregate is isotropic as discussed in Section II, it has been checked that the computed values of $\bar{E}$ are identical for tension in the two coordinate directions.

For the cubic crystal described by Eqs. (2.7) there is no thermal anisotropy, but the elastic anisotropy can still lead to stress singularities at triple-grain junctions. Such a cubic material, with $\omega_1 = -60°$, has been analyzed for $\Sigma_{22} > 0$ and $\Sigma_{11} = 0$, and distributions of the normal stress σ_n on the grain-boundary facet considered (*AF* in Fig. 9(*b*)) are shown in Fig. 11. The figure gives the stress distribution over half of the facet, emphasizing the part closest to the triple point *F*, where the mesh is refined (Fig. 10).

For $R = 1$ the cubic crystal is isotropic, which gives a uniform stress state with $\sigma_n/\Sigma_{22} = 1$ in the case analyzed. For $R = 1.5$ the anisotropy leads to a high stress peak at the triple point, and this could lead to microcrack nucleation in a very intense stress field such as that at the tip of a macroscopic crack.[7-9] On the other hand, for $R = 0.5$ the normal stress decays toward the triple point. Varying the value of Q in the range from ⅔ to 1 has less influence on the normal stress distribution. It is noted that these results agree perfectly with the singularity analysis (Fig. 3), which gives $\lambda > 0$ for $R < 1$, whereas the stress fields are singular ($\lambda < 0$) for $R > 1$.

The same analysis is carried out for an aggregate composed of orthotropic crystals characterized by Eqs. (2.5) and (3.4), again taking $\omega_1 = -60°$. Normal stress distributions on the grain-boundary facet in the vicinity of the triple point *F* are shown in Fig. 12 for uniaxial plane strain tension with no temperature change, $\Sigma_{22} > 0$, $\Sigma_{11} = 0$, $\Delta T = 0$. For $f = 1$ the grains are isotropic, which gives $\sigma_n/\Sigma_{22} = 1$. For $f = \sqrt{2}$, where the most stiff directions point toward the point *F* in all three grains adjacent to *F*, there is a significant stress increase at the triple point. In the opposite situation, where $f = 1/\sqrt{2}$, the normal stress on the facet decays toward the triple point. Also these results agree with the

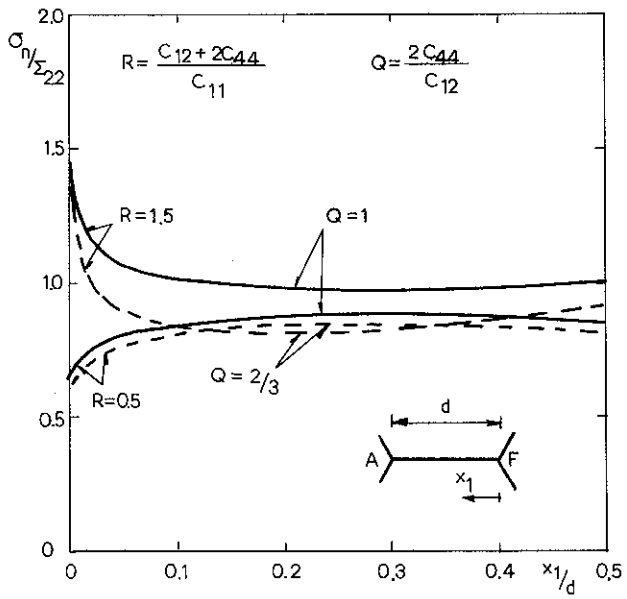

Fig. 11. Normal stresses σ_n on the grain-boundary facet *AF*, for a material composed of cubic crystals, subject to uniaxial plane strain tension.

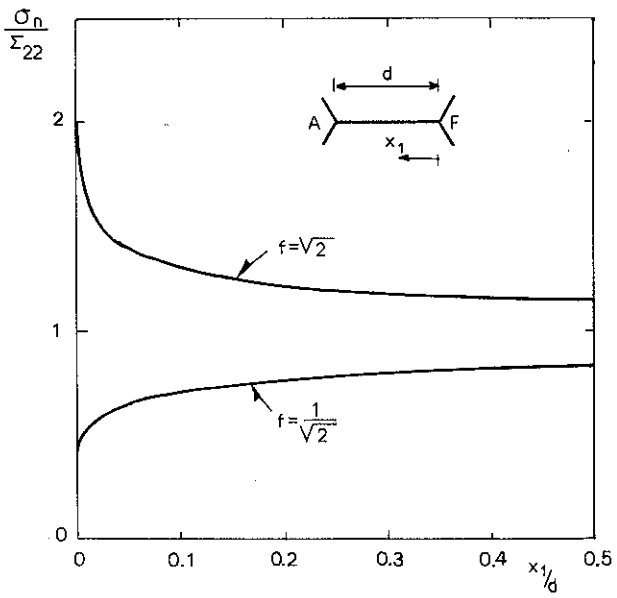

Fig. 12. Normal stresses σ_n on the grain-boundary facet *AF*, for a material composed of orthotropic crystals, specified by Eqs. (2.5) and (3.4), subject to uniaxial plane strain tension.

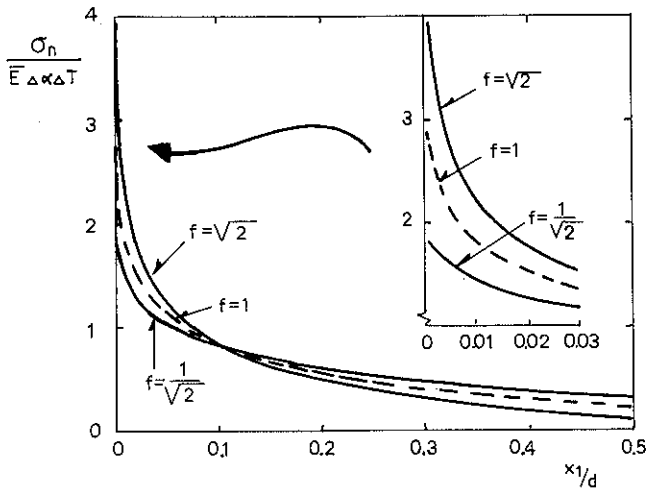

Fig. 13. Normal stresses σ_n on the grain-boundary facet AF, for a material composed of orthotropic crystals, specified by Eqs. (2.5), (2.6), and (3.4), subject to thermal contraction corresponding to the cooling range ΔT.

singularity analysis in Section III. Thus, Fig. 6 shows that there is a stress singularity ($\lambda < 0$) for $C_{11} > C_{22}$, whereas $\lambda > 0$ for $C_{11} < C_{22}$.

It is noted that the elastic anisotropies of the grains considered here do not model a particular ceramic. However, choosing $f = \sqrt{2}$ or $f = 1/\sqrt{2}$ means a factor 2 between the values of the stiffnesses C_{11} and C_{22}, and this factor is considered reasonably realistic, comparing with the values found for a number of crystals.[12,13]

In contrast to the cubic crystal, the orthotropic crystal considered in Fig. 12 does have thermal expansion anisotropy, as specified by Eq. (2.6). The residual stresses due to cooling, but in the absence of external loads, $\Delta T > 0$, $\Sigma_{11} = \Sigma_{22} = 0$, are shown in Fig. 13 for the polycrystal also considered in Fig. 5. These normal stresses are proportional to $\Delta\alpha\Delta T$, and the stresses are here normalized by the factor $\bar{E}\Delta\alpha\Delta T$, where $\bar{E}$ is the uniaxial plane strain tension modulus mentioned above. In this case elastic isotropy ($f = 1$) does give a stress singularity at the triple point F, as was also found by Evans[4] and Fu and Evans,[5] but a logarithmic singularity as opposed to the power-type singularity analyzed in Section III. The analysis of Fu and Evans[5] considers a few grains embedded in an infinite isotropic material, and the relative orientations of the directions of maximum contraction are not quite those considered in Fig. 13. However, it is noted that the result for $f = 1$ in Fig. 13 is of the order of magnitude expected, based on a comparable result of Fu and Evans.[5]

The stress distributions for $f = \sqrt{2}$ and $f = 1/\sqrt{2}$ in Fig. 13 show that the elastic anisotropy has a significant influence on the stress levels near the triple point. For $f = \sqrt{2}$ the normal stresses are smaller in the central part of the grain-boundary facet; but it is more significant that the stress level is increased near the triple point, since this is the location where microcracks are likely to be nucleated. Also the stress distributions at the other end of the facet, near point A, have been analyzed (by using $\omega_1 = 60°$ in the present computational scheme). However, here the stress level is lower, so that the value of $\sigma_n/(\bar{E}\Delta\alpha\Delta T)$ only exceeds unity over a short interval of about $0.002d$ near point A.

The increase of the residual stress peak found for $f = \sqrt{2}$ in Fig. 13 is even more interesting when seen in comparison with Fig. 12. The residual stresses are present in the material because of cooling from the fabrication temperature; but when loads are applied to the material, the stress concentration found in Fig. 12 is added to the residual stresses, and this stress concentration was not present in the elastically isotropic material. Thus, for $f = \sqrt{2}$ the two different effects of the elastic anisotropy add up, so that the likelihood of microcrack nucleation at the triple point is much increased.

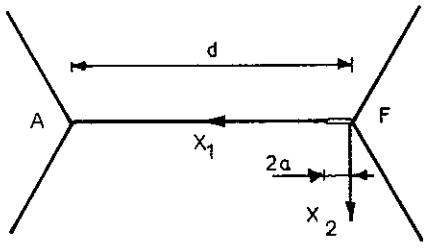

Fig. 14. Grain-boundary crack of length $2a$ at the triple point F.

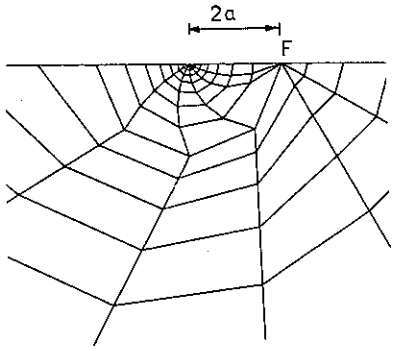

Fig. 15. Mesh in the near vicinity of the grain-boundary crack, applied in the computation for $2a/d = 0.05$.

V. Grain-Boundary Microcrack

The condition for the onset of grain-boundary microfracture depends on the size of small defects in the boundary. The most critical location of such defects is at the triple-grain junctions, where high stress peaks occur. To investigate the critical size of such defects, dependent on the grain size and the anisotropies, an analysis is carried out here for a small crack of length $2a$, extending from the triple point denoted by F in Figs. 1 and 9, as illustrated in Fig. 14. The crack tip at the triple point is essentially locked, but if the stress intensity factor at the other tip exceeds the fracture toughness for the grain boundary, the crack will grow to create a fully cracked grain-boundary facet.

In the numerical solution, the periodicities shown in Figs. 1 and 9 are still used, and the mesh at some distance from the crack is identical with that shown in Fig. 10(a). The mesh used near the crack is shown in Fig. 15 for a case where $2a/d = 0.05$. In this calculation the mesh consists of 22×6 elements. The six elements in the first ring around the crack tip to be investigated are wedge shaped, and the 13 nodes meeting at the tip are tied together as a single node. At the other end of the crack (the triple point F) four of the elements are wedge shaped, and also here the nodes are tied together. The boundary conditions (4.4) to (4.8) are unchanged, but Eqs. (4.3) have to be modified:

$$T_1 = T_2 = 0 \quad (\text{at } x_2 = 0,\ 0 < x_1 < 2a) \tag{5.1a}$$

$$T_1 = 0, \quad u_2 = 0 \quad (\text{at } x_2 = 0,\ x_1 \leq 0,\ x_1 \leq 0 \text{ or } x_1 \geq 2a) \tag{5.1b}$$

The stress intensity at the crack tip will here be characterized by the path-independent J integral (Rice[17]), which can be used for any material inhomogeneity that is independent of x_1, but may depend on x_2. In the x_α-coordinate system used here, J is defined by

$$J = \int_\Gamma (Wn_1 - \sigma_{ij}n_j u_{i,1})\, ds \tag{5.2a}$$

$$W(\varepsilon_{kl}) = \int_0^{\varepsilon_{kl}} \sigma_{ij}\, d\varepsilon_{ij} \tag{5.2b}$$

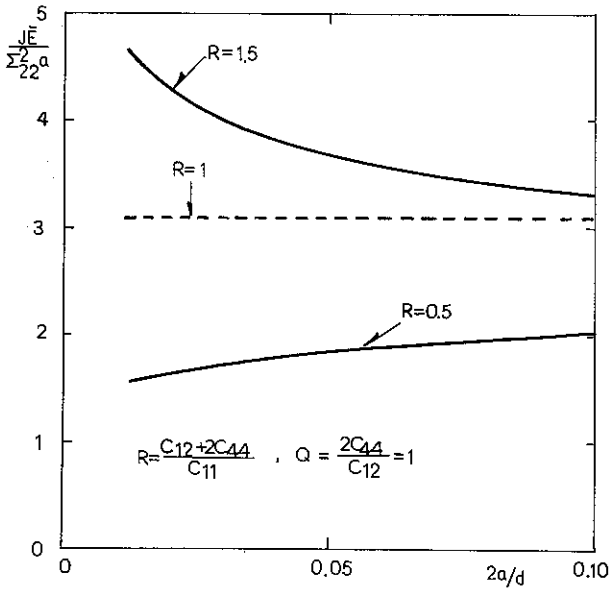

Fig. 16. J integral as a function of crack length, for a material composed of cubic crystals, subject to uniaxial plane strain tension.

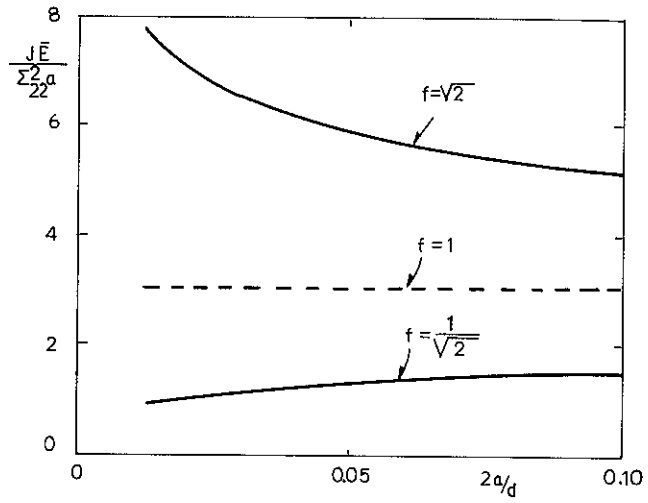

Fig. 17. J integral as a function of crack length, for a material composed of orthotropic crystals, specified by Eqs. (2.5) and (3.4), subject to uniaxial plane strain tension.

where Γ is any counterclockwise contour surrounding the crack tip, n_j is the outward normal to Γ, and ds is the arc length along Γ. The value of J for a crack tip is equal to the energy release rate, and this value can be compared with the grain-boundary fracture energy for a particular ceramic material, to check whether or not the size of the defect exceeds the critical crack length (Evans[4]).

First the aggregate composed of cubic crystals is analyzed, subject to uniaxial plane strain tension, $\Sigma_{22} > 0$, $\Sigma_{11} = 0$, $\Delta T = 0$. The relative orientations of the crystal axes are chosen as $\omega_1 = -60°$, and the anisotropies are characterized by R in Eq. (2.7b), choosing $Q = 1$ in the present cases. The cracks considered here are so small relative to their spacing that interaction can be neglected. Thus, in the isotropic case, $R = 1$, the value of the curve integral of Eqs. (5.2) should be directly given by the expression corresponding to an isolated crack, $J = \Sigma_{22}^2 \pi a(1 - \nu^2)/E$, where ν is Poisson's ratio and E is Young's modulus.

In the numerical calculations the integral of Eqs. (5.2) is evaluated on contours that follow the rings of elements around the crack tip (see Fig. 15), where each contour passes through the central integration points of the elements. The J integral is evaluated for six different contours, and the average value is used in Fig. 16. It is noted that the maximum deviation from this average value is about 2%, which confirms the path independence of Eqs. (5.2). Furthermore, for the isotropic case, $R = 1$, the average J value deviates at most 2% from the value of the expression given above for an isolated crack. A better approximation could be obtained by a finer mesh, but the present accuracy is considered sufficient.

For anisotropic cubic crystals, with $R = 1.5$, Fig. 16 shows that the value of the ratio J/a increases when $2a/d$ decreases. Thus, in a given stress state a crack of a given length $2a$ is more severe the larger the grain size. This was also expected based on the stress distributions shown in Fig. 11, since a smaller crack relative to the facet length d is more engulfed in the highly stressed region near the triple point. For $R = 0.5$ the opposite effect is found, as also expected based on Fig. 11.

Figure 17 shows values of J for an aggregate composed of the orthotropic crystals characterized by Eqs. (2.5) and (3.4), under uniaxial plane strain tension, $\Sigma_{22} > 0$, $\Sigma_{11} = 0$, $\Delta T = 0$, and for $\omega_1 = -60°$. Again, the values found for the isotropic material, $f = 1$, deviate less than 2% from the J value corresponding to an isolated crack. The anisotropy described by $f = \sqrt{2}$ increases the value of J significantly, so that J is more than doubled for $2a/d < 0.04$. This is a much stronger effect of elastic anisotropy than that found in Fig. 16. On the other hand, the anisotropy characterized by $f = 1/\sqrt{2}$ gives a reduced energy release rate, which also agrees with the stress distribution found in Fig. 12.

The effect of thermal expansion anisotropy is illustrated in Fig. 18, for an aggregate subject to cooling, $\Delta T > 0$, but no external loads, $\Sigma_{11} = \Sigma_{22} = 0$. Here, the value of J/a increases for decreasing $2a/d$, even in the case of isotropic elastic behavior, $f = 1$, as would be expected since the corresponding stress distribution in Fig. 13 has a singularity at the triple point (see also Evans[4]). The values of J are also here significantly increased by the elastic anisotropy characterized by $f = \sqrt{2}$, and the values are decreased for $f = 1/\sqrt{2}$.

The expression (Eqs. (5.2)) for the J integral is not directly applicable under a temperature change. However, it is seen that the expression still applies when ε_{ij} and $u_{i,1}$ are replaced by $\varepsilon_{ij} - \varepsilon_{ij}^T$ and $u_{i,1} - u_{i,1}^T$, respectively, where ε_{ij}^T are the thermal contraction strains, $u_{i,1}^T = \varepsilon_{11}^T$ and $u_{2,1}^T = 0$.

It was already noted above that the increased stress levels found for $f = \sqrt{2}$ in Figs. 12 and 13 add up when a ceramic material, which contains residual stresses due to cooling from the fabrication temperature, is also subjected to external loading. The same effect is clearly seen from Figs. 17 and 18. For both types of loading the elastic anisotropy characterized by $f = \sqrt{2}$ has the effect that the value of the ratio J/a is significantly increased. For a given value of the grain-boundary fracture energy this means that the critical size of a defect that will result in a fully cracked grain-boundary facet is significantly smaller in the material with elastic anisotropy.

VI. Discussion

The predictions of the two-dimensional model of a polycrystal analyzed here can be compared with observed critical grain sizes for spontaneous fracture, reported by Rice and Pohanka.[3] For Al_2O_3 the thermal expansion anisotropy is[3] $\Delta\alpha \simeq 0.55 \times 10^{-6}$ °C^{-1} and the uniaxial plane strain tension modulus of the aggregate is $\bar{E} \simeq 3.6 \times 10^5$ MN/m^2. The grain-boundary fracture energy γ_{gb} is well below the fracture energy for the uncracked polycrystal, and here we will assume[3,4] $\gamma_{gb} \simeq 1$ J/m^2. Cooling from the fabrication temperature gives $\Delta T \simeq 1000$°C, and furthermore the largest defects observed in a polycrystal that has not cracked spontaneously are $2a \simeq 0.02d$. Using these values and the fracture criterion $J_c = 2\gamma_{gb}$, the curve for $f = 1$ in Fig. 18 gives the critical facet size $d_C \simeq 216$ μm at spontaneous fracture, which is in reasonable agreement with the critical grain size of about 400 μm observed experimentally.[3] Thus, the predictions of the

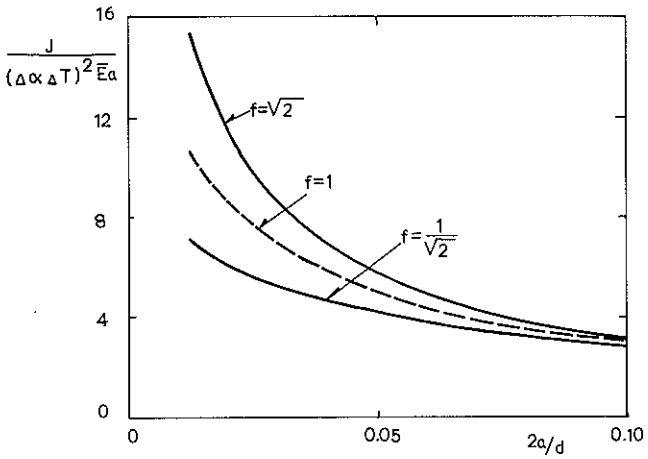

Fig. 18. J integral as a function of crack length, for a material composed of orthotropic crystals, specified by Eqs. (2.5), (2.6), and (3.4), subject to thermal contraction corresponding to the cooling range ΔT.

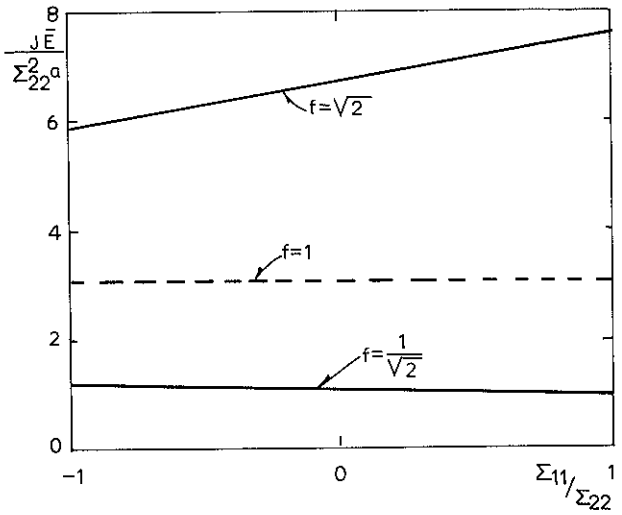

Fig. 19. J integral as a function of the applied stress Σ_{11} in the direction tangential to the crack. The crack length is $2a = 0.025d$, in a material composed of orthotropic crystals, specified by Eqs. (2.5) and (3.4), subject to a biaxial plane strain tension.

two-dimensional model of a polycrystal are of the right order of magnitude.

The present investigation has shown that elastic anisotropy of the grains can significantly affect the values of the applied load or the cooling range that result in grain-boundary cracking. Both the asymptotic analysis for the stress field near a triple-grain junction and the numerical analyses show that the elastic anisotropy can result in a stress singularity at the triple point, or in stresses that decay toward zero, dependent on the relative orientations of the crystal axes in the grains adjacent to the triple point. A significant effect of the elastic anisotropy is that in a location where it amplifies the stresses due to thermal contraction anisotropy, it also amplifies the stresses due to external loading, so that these two stress increases add up. For the order of magnitude of the deviations from isotropy that are relevant, the increase of the energy release rate for the tip of a grain-boundary defect can typically be a factor of 2.

Elastic anisotropy of the grains has the additional effect that it results in an influence of multiaxial stress states on microcrack nucleation. This is illustrated in Fig. 19, which shows the variation of the J integral with the stress Σ_{11} in the direction tangential to a grain-boundary crack with length $2a = 0.025d$. For $\Sigma_{11} = 0$ these results are identical with those shown in Fig. 17, corresponding to $2a/d = 0.025$. In an isotropic solid it is well-known that for a given applied stress normal to the crack the value of the stress intensity factor is independent of the mean stress, as also shown for $f = 1$ in Fig. 19; but this is not the case for anisotropic crystals ($f \neq 1$). Thus, for $f = \sqrt{2}$, where it has been found that the elastic anisotropy amplifies the stress peak, the value of the J integral is further increased by a tensile stress Σ_{11} tangential to the crack. This is important in the highly stressed region around the tip of a macroscopic crack, where the high level of triaxial tension will then further increase the likelihood of microcrack nucleation.

APPENDIX

Plane Strain Singularity Analysis at a Grain-Boundary Triple Point

The singularity analysis leading to stresses of the form of Eq. (3.2) is now well-known, so here only a very brief outline of the analysis will be given. The radial and circumferential components of the displacement, u and v, are used as the dependent variables and a separated solution of the form

$$(u, v) = kr^{\lambda+1}(\tilde{u}(\theta), \tilde{v}(\theta)) \qquad \text{(A–1)}$$

is sought. In each sector at the junction (see Fig. 2) the equilibrium equations are expressed in terms of the displacments via the strain–displacement relations and the constitutive equations (3.1). The resulting ordinary differential equations for $\tilde{u}$ and $\tilde{v}$ can thereby be reduced to a set of four first-order equations in the form

$$y' = A(\lambda, \theta)y \qquad \text{(A–2)}$$

where $y = (\tilde{u}', \tilde{v}', \tilde{u}, \tilde{v},)$, $(\ )' = d(\ )/d\theta$, and where A is a 4×4 matrix with coefficients which depend on λ and θ.

Jump conditions across the radial grain boundary at $\theta = 120°$ follow from continuity of tractions and displacements and can be expressed as $y^+ = By^-$ where B is a 4×4 matrix also depending on λ. These equations together with homogeneous symmetry (or antisymmetry) conditions at $\theta = 0$ and π constitute an eigenvalue problem for λ and the associated $y(\theta)$. A standard finite-difference procedure was used to solve for the physically relevant eigenvalues and eigenmodes. The eigenvalues λ were computed to at least four-place accuracy.

Acknowledgments: This work was carried out while J.W.H. was visiting at the Department of Solid Mechanics of the Technical University of Denmark.

References

[1] J. A. Kuszyk and R. C. Bradt, "Influence of Grain Size on Effects of Thermal Expansion Anisotropy in $MgTi_2O_5$," *J. Am. Ceram. Soc.*, **56**, 420–23 (1973).
[2] J. J. Cleveland and R. C. Bradt, "Grain-Size/Microcracking Relations for Pseudobrookite Oxides," *J. Am. Ceram. Soc.*, **61**, 478–81 (1978).
[3] R. W. Rice and R. C. Pohonka, "Grain-Size Dependence of Spontaneous Cracking in Ceramics," *J. Am. Ceram. Soc.*, **62**, 559–63 (1979).
[4] A. G. Evans, "Microfracture from Thermal Expansion Anisotropy—I. Single Phase Systems," *Acta Metall.*, **26**, 1845–53 (1978).
[5] Y. Fu and A. G. Evans, "Some Effects of Microcracks on the Mechanical Properties of Brittle Solids—I. Stress, Strain Relations," *Acta Metall.*, **33**, 1515–23 (1985).
[6] J. T. Fredrich and T.-F. Wong, "Micromechanics of Thermally Induced Cracking in Three Crustal Rocks," *J. Geophys. Res., B*, **91** [12] 12,743–12,764 (1986).
[7] M. Rühle, A. G. Evans, R. M. McMeeking, P. G. Charalambides, and J. W. Hutchinson, "Microcrack Toughening in Alumina/Zirconia"; unpublished work.
[8] J. W. Hutchinson, "Crack Tip Shielding by Micro-cracking in Brittle Solids"; to be published in *Acta Metall.*
[9] M. Ortiz, "A Continuum Theory of Crack Shielding in Ceramics," *J. Appl. Mech.*, **54**, 54–58 (1987).
[10] R. M. McMeeking and A. G. Evans, "Mechanics of Transformation Toughening in Brittle Materials," *J. Am. Ceram. Soc.*, **65**, 242–46 (1982).
[11] W. Boas and R. W. K. Honeycombe, "The Plastic Deformation of Non-cubic Metals by Heating and Cooling," *Proc. R. Soc. London, A*, **186**, 57–71 (1946).

[12]American Institute of Physics Handbook, 2nd ed. Edited by D. E. Gray. McGraw-Hill, New York, 1963.
[13]G. Simmons and H. Wang, Single Crystal Elastic Constants and Calculated Aggregate Properties: A Handbook, 2nd ed. MIT Press, Cambridge, MA, 1971.
[14]M. L. Williams, "Stress Singularities Resulting from Various Boundary Conditions in Angular Corners of Plates in Extension," *J. Appl. Mech.*, **19**, 526–28 (1952).
[15]V. Tvergaard, "Effect of Thickness Inhomogeneities in Internally Pressurized Elastic-Plastic Spherical Shells," *J. Mech. Phys. Solids*, **24**, 291–304 (1976).
[16]C. F. Shih and A. Needleman, "Fully Plastic Crack Problems, Part I: Solution by a Penalty Method," *J. Appl. Mech.*, **51**, 48–56 (1984).
[17]J. R. Rice, "A Path Independent Integral and the Approximate Analysis of Strain Concentration by Notches and Cracks," *J. Appl. Mech.*, **35**, 379–86 (1968). □